Andressa Antunes Bortoti[a,b,c], Amanda de Freitas Gavanski[a], Yegraf Reyna Velazquez[b,c], Andressa Galli[a], Eryza Guimarães de Castro[a,*]

[a] Universidade Estadual do Centro-Oeste – UNICENTRO, Departamento de Química, Campus CEDETEG, Guarapuava, PR, Brazil [b] Catalan Institute of Nanoscience and Nanotechnology (ICN2), Campus UAB, Bellaterra 08193, Barcelona, Spain [c] Barcelona Institute of Science and Technology (BIST), Campus UAB, Bellaterra 08193, Barcelona, Spain

ARTICLEINFO

Keywords: α-MoO_3
Characterization
Organic photovoltaic
Synthesis

ABSTRACT

This study describes a facile low cost route to synthesize the α-MoO_3 through a conversion of the precursor MoS_2 in oxidant media. The structure and morphology of the α-MoO_3 were studied by high resolution transmission electron microscopy (HRTEM) and selected area electron diffraction (SAED), X-ray diffraction (XRD), X-ray photoelectron spectroscopy (XPS) and Raman spectroscopy. The results show that α-MoO_3 was obtained with reduced size, high purity, strongly-preferred orientation and structural defects, which ensures versatility and multifunctionality to this sample. For the purpose of applications, α-MoO_3 was successfully employed in inverted organic solar cells devices as a possible alternative to the PEDOT:PSS in the hole transportation layer.

1. Introduction

Being a versatile material and widely used in industry, the molybdenum trioxide (MoO_3) has been subject of many studies over the past decade. An important layered oxide, MoO_3 presents attractive multifunctional properties, and have attracted considerable interest in many different applications, such as oxidative alcohols catalysis [1] and degradative dyes photocatalysis [2], also in batteries with other ions [3,4], sensors gas [5] and solar cells [6].

The molybdenum trioxide has a rich polymorphism that includes the orthorhombic phase (α-MoO_3) which is the only thermodynamically stable phase. This phase shows white or gray color, both with a layered structure formed by the MoO_6 octahedrons chains, which are interconnected by the corners linked along the [100] direction and sharing the edges along the [001] direction to form double layer sheets. The double layer sheets are stacked together by the weak van der Waals forces [7]. The other polytypes are the metastable monoclinic (β-MoO_3) and hexagonal (h-MoO_3) phases [8].

Due to its high hole mobility, good environmental stability and electronic properties, the MoO_3 is a promising and highly attractive candidate to replace the poly3,4-ethylene dioxythiophene: polystyrene sulphonic acid (PEDOT:PSS) in organic solar cells [6,9] and other electronic devices [10]. The most employed material as hole transportation layer (HTL) for organic solar cells is PEDOT:PSS which, in general, needs to be doped [6]. Unfortunately, PEDOT:PSS is identified as a major source of degradation in photovoltaic devices due to its acidic, the aggregation of particles in the water solution and hygroscopic nature [11]. A frequently employed strategy to solve this issue is to invert the layer sequence and also replace PEDOT:PSS by a more stable alternative material like MoO_3.

The usual way to achieve a coating layer of MoO_3 in solar cells is solution-processing or thermal evaporation [12]. Thermal evaporation shows a disadvantage for large scale production, that would be very expensive since requires special conditions while solution-processing is a low temperature procedure, which is important to avoid the active layer degradation [13,14]. For application in solar cells, inexpensive methods of synthesis of MoO_3, which produces stable materials with long lifetime, are essential.

Common solution processing methods used to synthesize the MoO_3 are the wet chemical methods like hydrothermal [14], solvothermal [15] and others [16,17]. These methods are able to produce more purified oxides, use inexpensive reagents, require simple equipment and provide materials with controlled morphology [18]. In the literature, there are no reports of the use of molybdenum disulfide (MoS_2) as a precursor for MoO_3. The MoS_2, also known as molybdenite, is a promising material for electronic industry [19], besides being the main natural source of molybdenum mineral.

In the present research, α-MoO_3 was synthesized from the facile conversion oxidative of MoS_2, using the wet chemical process. The physical and chemical properties were investigated by several characterization techniques and its performance in inverted solar cells was evaluated as a possible alternative to the PEDOT:PSS as the hole transportation layer, in inverted polymer solar cells.

2. Experimental

2.1. MoO_3 synthesis

In this process, only analytical grade chemical reagents, from Sigma Aldrich were used without further purification. The α-MoO_3 was prepared as follows: a dispersion of 0.0097 mo lL^{-1} of MoS_2 (particles < 2 μm) in HNO_3 (1.0 mol L^{-1}) was kept under reflux for about 150 min. After this time, 1 mL of concentrated H_2SO_4 was added and this mixture was kept under reflux at 85 °C, during additional 30 min. Finally, the refluxed material was centrifuged, washed three times with distilled water and dried at 60 °C in an electric oven for 24 h. This material was named MoO_3_Cz.

2.2. Characterization

The MoO_3_Cz structure was characterized by X-ray diffractometry (XDR), in a Bruker D2 Phaser equipment, using CuKα (λ=0.15418 nm) and 2θ scanning rate of 0.1° s^{-1} in the 2θ range of 10–50°. The morphology was investigated by high resolution transmission electron microscopy (HRTEM) and selected area electron diffraction (SAED), performed by a JEOL microscope, JEM-2011 operated at 200 kV and scanning electronic microscopy (SEM), performed by microscope TM3000 Hitachi. For HRTEM analysis, the sample powder was sonicated in ethanol during 15 min and the resulting suspension was dropped onto carbon-coated copper grids. Raman spectra were obtained on a Raman Renishaw 3000 Microprobe System, coupled to an optical microscope, focusing the incident radiation on a 1 μm spot, using a 514 nm laser as excitation source with incidence potency of 0.2 mW. Xray photoelectron spectroscopy (XPS) was done with the Al Kα (1486.6 eV). All spectra were adjusted according to the value of the C 1s peak at 284.4 ± 0.1 eV. The fitting was done using a Gaussian model on CASA application Software. The ultraviolet photoemission spectroscopy (UPS) was obtained using a He lamp (He l 21.2 eV) at an experimental resolution of 0.15 eV. The samples were biased at 3–5 V. Both

* Corresponding author.
E-mail address: eryza.castro@gmail.com (E.G. de Castro).

.

analyses (XPS/UPS) were done with equipment from SPECS using an energy analyzer PHOIBOS 150. The UV−VIS−NIR spectra in the absorbance mode were collected directly from solid sample in an Ocean Optics USB-2000 spectrophotometer.

2.3. Preparation of inverted organic solar cells

First, a MoO_3_Cz dispersion was prepared with 10 mg of MoO_3_Cz in 1 mL of distilled water. The inverted organic solar studied in the work has the structure glass/FTO/ZnO/P3HT:$PC_{60}BM$/MoO_3_Cz/Ag. The FTO substrate was supplied by SOLEMS (resistance: 70−100 Ω/□), it was pre-cleaned in a ultrasonic bath with detergent and then cleaned in deionized water, acetone and isopropanol respectively, for 10 min each and finally dried with a nitrogen stream. The FTO substrates were then subjected to a UV-ozone treatment for 20 min. The first layer of ZnO was deposited by sol gel spin coating method (3000 rpm for 40 s) onto the FTO substrate, following the sol gel synthesis method described by Andersen and colleagues [20]. After deposition, the ZnO film was sintered at 140 °C for 30 min. Then the active layer formed using a solution of poly (3-hexylthiophene) (P3HT) (Merck, 98%) and phenyl-C61-butyric acid methyl ester ($PC_{60}BM$) (Solenne, 99.5%) in chlorobenzene (Sigma-Aldrich) at a concentration of 30 mg/mL. This coating solution was dropped onto substrate (FTO/ZnO) using a spin coater operated at 1000 rpm. The next layer deposited was the mixture of MoO_3_Cz dispersion previously prepared with acetone (1:1). It was deposited onto active layer by spin coater at 1000 rpm and then dried at 120 °C for 10 min to evaporate de solvent. Finally, the last layer consisted of 100 nm thin film of Ag back metal electrode, which was deposited by thermal evaporation in an evaporation system (Auto 306, Broc Edwards), operating with a base pressure of 10^{-7} Pa at a deposition rate of 0.1 nm s^{-1}. The devices were subsequently annealed at 120 °C for 10 min in air.

For a comparative analysis, a similar cell was prepared as described previously, except for replacing the hole transportation layer MoO_3_Cz with PEDOT:PSS, i.e., poly (3,4- ethylenedioxythiophene) poly (styrenesulfonate). For this cell, the PEDOT:PSS (Clevious P VP AI 4083) was added to 0.70 µL of Triton-100X and ethyleneglycol (1:1) mixture. Both reagents were purchased from Sigma Aldrich.

2.3.1. Solar cells characterization

The solar simulation was carried out using a Steuernagel Solarkonstant KHS1200 system. Light Intensity was adjusted at 1000 W/m^2 with a bolometric Zipp & Konen CM-4 pyranometer.

Calibration of the sun simulator was carried out by several means, i.e., with a calibrated S1227-1010BQ photodiode from Hamamatsu and a minispectrophotometer from Ava-Spec 4200. The AM1.5G reference spectrum was according to the ASTM G173 standard. Solar decay and IV-curves were measured using a Keithley 2601 multimeter connected to a personal computer.

3. Results and discussion

3.1. Characterization of MoO_3

Fig. 1 contains the diffractograms of precursor MoS_2, MoO_3 commercial and the MoO_3 sample obtained in this study. The difftactogram of MoS_2, Fig. 1a, shows the diffraction peaks characteristic of the 2 H polymorph 2θ=14.40, which correspond to a interlayer distance of 6.15 Å [21]. The commercial oxide diffractogram (Fig. 1b) was used as a comparative of the crystalline structure. In both MoO_3 samples analyzed (Fig. 1b and c), the crystalline structures were identified as α polymorph type [22], where all diffraction peaks could be indexed according to the standard PDF n° 00-0 05-0508. It should be noted in the Fig. 1c that the intensities in the (0k0) planes, with k=2, 4 and 6, were higher than the commercial MoO_3, indicating that the MoO_3_Cz sample, obtained by reflux, showed a highly anisotropic structure [23], with preferential orientation in the [001] direction [24]. The observed peaks broadening in the synthesized MoO_3_Cz was attributed to the size effect, suggesting the presence of small particles. No obvious diffraction patterns for other phases were found in this

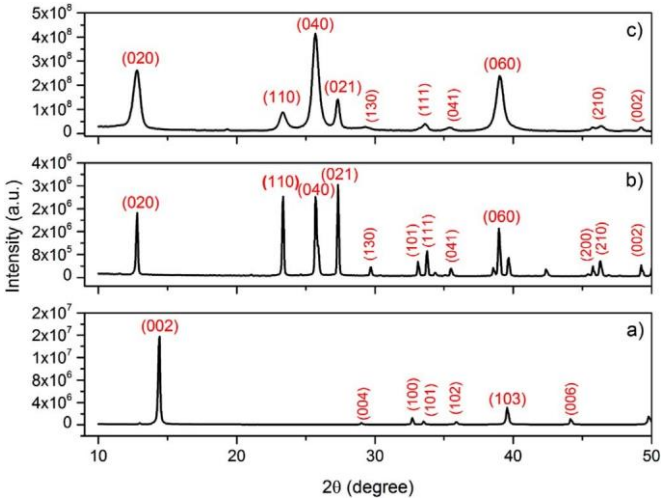

Fig. 1. XRD patterns of the precursor MoS_2 (a), α-MoO_3 commercial (b) and αMoO_3_Cz (c).

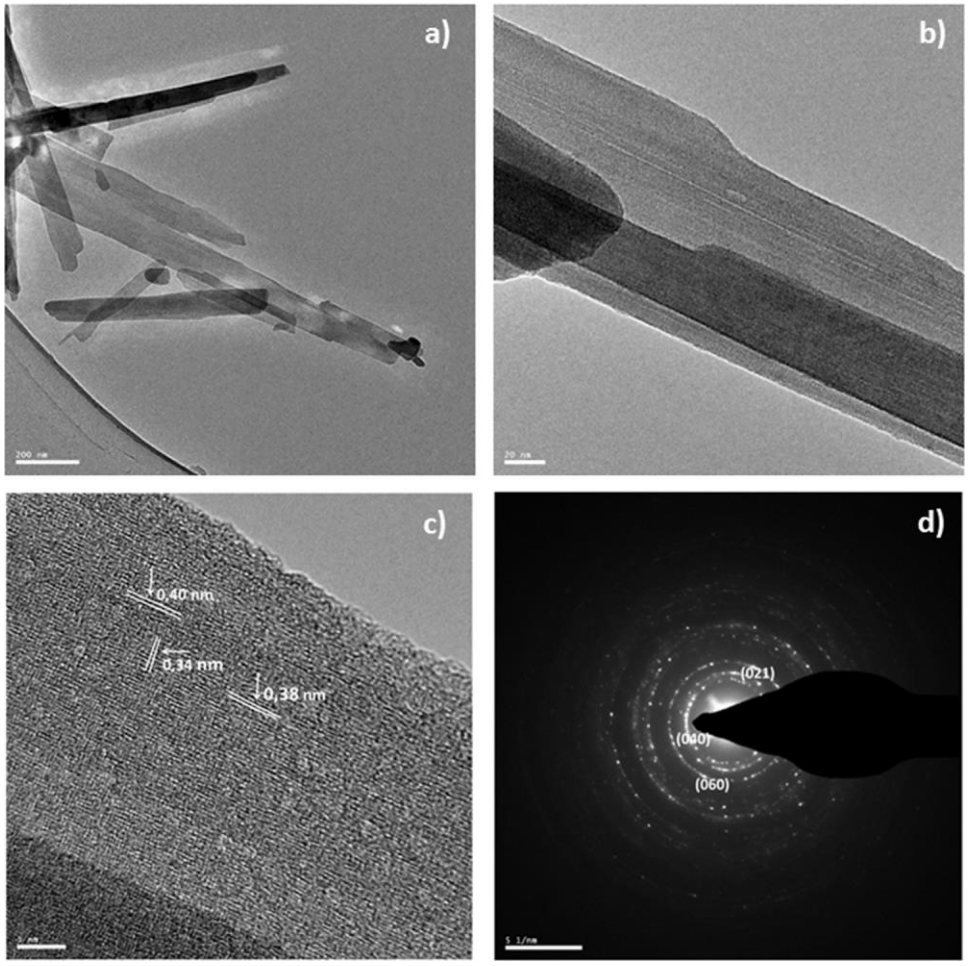

Fig. 2. HRTEM images of the MoO_3_Cz (a-c), and SAED image of the MoO_3_Cz (d).

sample, indicating that MoS_2 were completely converted to the oxide.

The morphology of the prepared MoO_3_Cz was examined by HRTEM. As can be seen in the Fig. 2a-c, it was possible to observe the belt-type morphology of MoO_3_Cz, with belt length of about 3 μm and width smaller than 200 nm, proving the preferential growth previously identified by X-ray diffraction peak (004) [25,26]. The thickness of the belts was probably in nanoscale, however, the characterization techniques used in this study did not permit to determine precisely this thickness. The morphology of MoS_2 precursor can be seen in the Fig. 2d. Different methods used to synthesize MoO_3 belts, described by other authors, using acid as an oxidizing means are compared in Table 1. The present work is advantageous compared to the others synthetic routes, because of the simplicity since it does not use an autoclave, the synthesis time is reduced and produces smaller particles than founded in previously reported work. Fig. 2c shows the fringes of the crystal lattice, with spacing of 0.34 nm and 0.38 nm, corresponding to the interplanar distance of (040) and (110) planes, of the α-MoO_3, respectively. This images also revealed structural defects, which were clearer in the direction of (110) plane, in which some regions were spaced with different sizes of the pattern. The selected area electron diffraction (SAED) pattern, given in Fig. 2e, revealed the polycrystalline nature indicated by diffraction rings and defined points [27]. The assignments of diffraction rings were in agreement with the crystallographic card PDF 00-005-0508. In addition, these images revealed that there were many structural defects on the surface of MoO_3_Cz indicated by diffraction in many ways, Fig. 2c [2,27].

The Raman spectra of MoS_2, MoO_3 and MoO_3_Cz are shown in the Fig. 3, and were obtained under the same conditions. The MoS_2 spectra (Fig. 3a) showed two main bands centered at 383 and 408 cm^{-1}, assigned to S-Mo-S vibrational modes [19,29,30]. It is important to emphasize that the lower laser power was used to prevent the conversion of the MoS_2 to MoO_3. The Raman spectrum of MoO_3_Cz, Fig. 3b, was similar to commercial MoO_3 spectrum (Fig. 3c). These spectra consist of bands in the 400−200 cm^{-1} region (242, 289, 336, e 379 cm^{-1}) that were attributed to the bending modes of the orthorhombic α-MoO_3 crystalline phase. The presence of these peaks indicated a distorted octahedron and could be assigned to the Mo^{6+}=O stretching mode of terminal oxygen atoms, which were

Table 1
The α-MoO_3 belts synthetized by acid reaction.

Mo Sources	Reagents	Temperature (°C)	Time	Requirement	length (μm)	width (μm)	Ref
molydenyl acetylacetone	HNO_3	200	20 h	Autoclave	200	40	[25]
Na_2MoO_4	HCl	140	24 h	Autoclave	8	0.5	[15]
Na_2MoO_4	HBF_4	180	24 h	Autoclave	3,00	0.3	[28]
$(NH_4)_6Mo_7O_{24}$	HNO_3	180	20 h	Autoclave	> 10	< 0.2	[23]
MoS_2	HNO_3	85	3 h	Free	2	> 0.2	This work

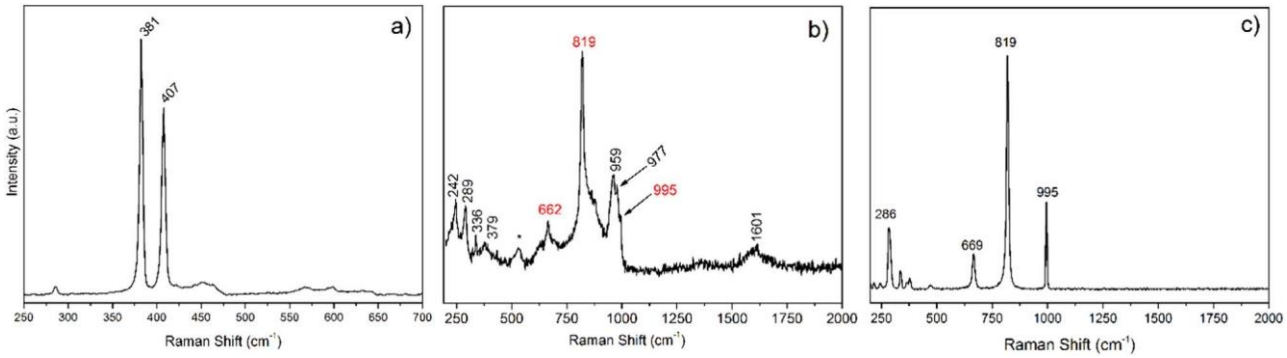

Fig. 3. Raman spectral (λ=514 nm) of the MoS2 precursor (a), MoO_3_Cz (b) and MoO_3 commercial (c), obtained with samples deposited on Si substrate. (For clear observation, the peak at 521 cm^{-1}, identified by *, is attributed to Si).

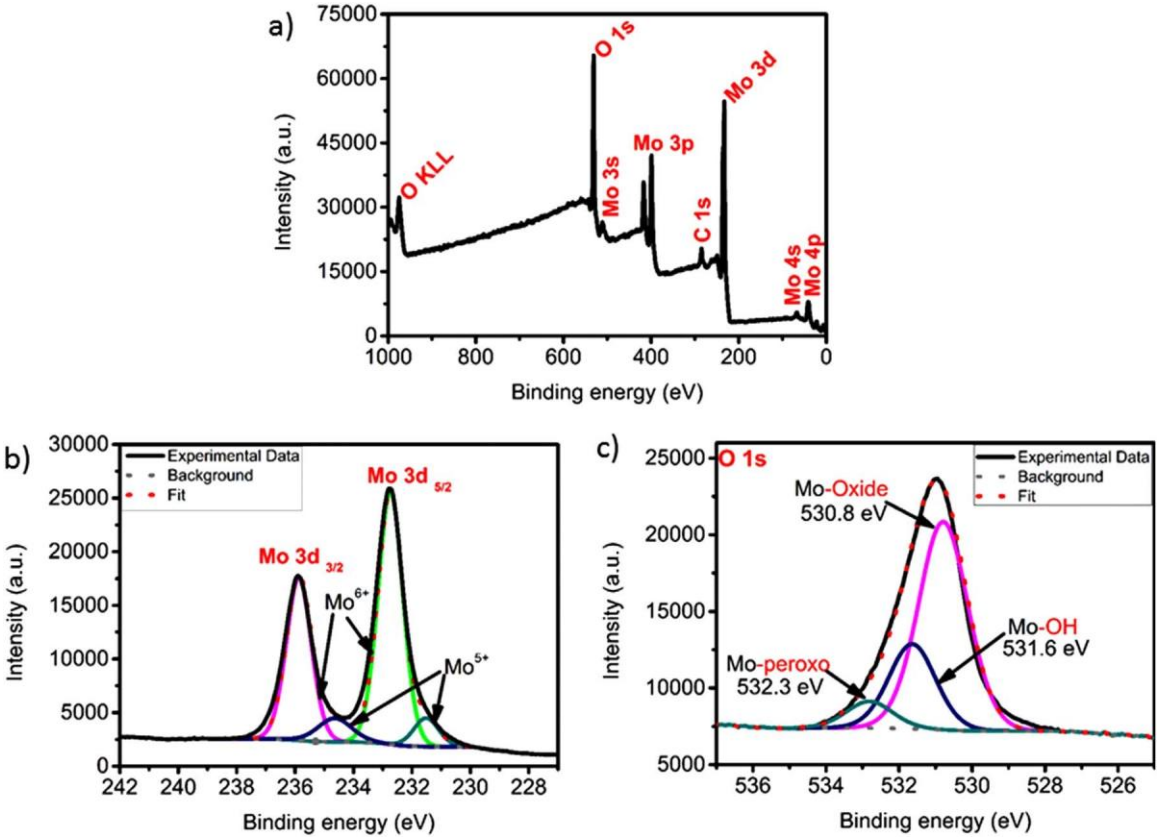

Fig. 4. XPS of MoO_3_Cz (a) survey spectrum, Mo 3d (b) and O 1 s (c) core level regions.

Table 2
Values provided by CasaXPS software related to the deconvolution of the Fig. 4b and c.

	Attribution	Position	Area	% Atom
O 1s	Oxide	530.79	9590.1	47.66 ± 1.30
O 1s	OH	531.64	3684.9	18.31 ± 4.44
O 1s	Peroxo	532.81	1155.5	5.74 ± 0.91
Mo $3d_{5/3}$	Mo_{6+}	232.74	9786.7	15.00 ± 0.50
Mo $3d_{3/2}$	Mo_{6+}	235.87	6313.3	9.68 ± 0.51
Mo $3d_{5/3}$	Mo_{5+}	231.51	1103	1.69 ± 0.41
Mo $3d_{3/2}$	Mo_{5+}	234.64	1247.6	1.91 ± 0.92

created from breaking of Mo_2–O bonds at the corner-shared [31]. Specifically, the peaks at 336 and 379 cm^{-1} were assigned to O-Mo-O bending and scissoring vibrations respectively and the 244 cm^{-1} peak was due to the O=Mo=O twist modes [32]. Additional intense bands were also seen at 995, 819 e 662 cm^{-1}, corresponding to the characteristic nature of the orthorhombic α-MoO_3 phase which was in agreement with the XRD data [31]. These bands were an indicative of the organization degree of the material structure, which matched with more organized structure [33]. The band at 995 cm^{-1} was assigned to the asymmetric stretching mode of terminal oxygen (Mo^{6+}=O) along the a and b axes which would result from an unshared oxygen and it would be responsible for the layered structure of α-MoO_3 [31,34]. The band at 819 cm^{-1}, was assigned to the doubly coordinated oxygen (Mo_2-O) symmetric stretching mode, which resulted from cornershared oxygen, common to two MoO_6 octahedral [31]. The band at 662 cm^{-1} was assigned to asymmetric stretching mode of triply coordinated oxygen (Mo_3-O) along the c-axis, resulting oxygen atom at the edge of the shared structure, with three adjacent MoO_6 octahedral [34]. It can be seen that the bands from MoS_2 did not appear in the spectrum, indicating that the precursor was completely converted to oxide and it was in agreement with the XRD data. We believe that small differences observed in the Raman spectrum of MoO_3_Cz and MoO_3 commercial could be due to structural defects in

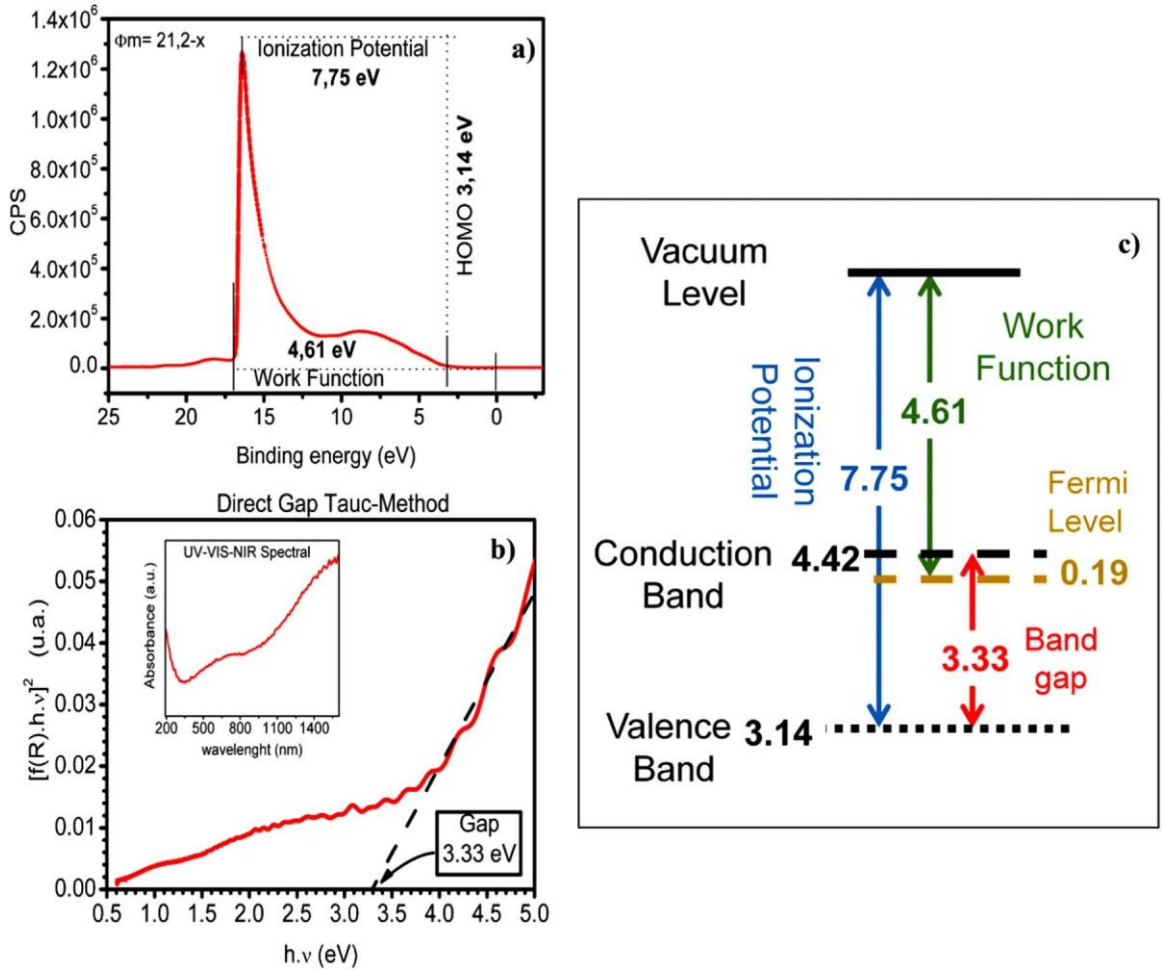

Fig. 5. (a) UPS spectra, referenced to vacuum level. (b) Tauc's method applied to UV–VIS–NIR spectrum (inset) and (c) energy level diagram for MoO_3_Cz.

Table 3
Experimental data from inverted organic solar cell with MoO_3_Cz at different speed of spin coating.

Deposition Speed (rpm)	V_{oc} (V)	J_{sc} (mA cm-2)	FF (%)	PCE (%)
500	0.397 ± 0.158	7.821 ± 1.099	33.206 ± 5.455	1.173 ± 0.644
1000	0.502 ± 0.019	7.386 ± 0.810	37.002 ± 2.344	1.371 ± 0.162
2000	0.398 ± 0.026	7.892 ± 0.732	33.249 ± 1.431	1.123 ± 0.173
3000	0.484 ± 0.108	8.214 ± 1.186	33.492 ± 3.744	1.331 ± 0.487

Table 4
Experimental data of inverted organic solar cell com paring between MoO_3 EDOT:PSS such as hole transporter layer.

HTL	V_{oc} (V)	J_{sc} (mA cm^{-2})	FF (%)	Rsh (Ω cm^2)	Rs (Ω cm^2)	PCE (%)
MoO_3_Cz	0.521	7.386	40.318	4.80 ± 0.17	24.05 ± 1.44	1.553
PEDOT:PSS	0.443	7.541	33.99	10.47 ± 0.32	28.65 ± 0.8	1.135

MoO_3_Cz [3], such as indicated by the HRTEM.

In the XPS spectra of the MoO_3_Cz sample (given in Fig. 4a), it may be noted that there were only signals for carbon, oxygen and molybdenum. These data corroborated the XRD and Raman analysis regarding the phase purity of the obtained material. The Table 2 provides the extracted values of CasaXPS software relative to the graphic present in the Fig. 4b and c. A typical signal of Mo^{6+} can be seen in the Fig. 4b [31,35]. The binding energies at 232.7 eV and 235.8 eV, exhibited doublet-spin signals corresponding to Mo $3d_{5/2}$ and Mo $3d_{3/2}$, respectively. Based on the deconvolution of the peaks, another weaker doublet appeared with peak maxima at binding energy of around 231.4 eV and 234.6 eV, which is assigned to the Mo $3d_{5/2}$ and Mo $3d_{3/2}$ of the Mo^{5+} ion [33,35]. The calculated percentage of Mo^{5+}, based on the area under de correspondent peaks of Mo^{6+} and Mo^{5+}, was 15%. The presence of Mo^{5+} can related to deficiency of oxygen (vacancy) indicating surface defects [36,37], agreeing with HRTEM data. The Fig. 4c shows the XPS spectrum of the O 1s, with characteristic sign at 530 eV. The deconvolution of the peaks indicated the presence of an intense peak at 530.8 eV that could be attributed to O 1s of the Mo-O bond [35], and two lower intensity peaks at 531.6 eV and 532.3 eV. The peak at 531.6 eV could be attributed to interstitial oxygen atoms of the MoO_3 surface [32], in the hydroxyl

groups form (-OH), which were incorporated on the surface by the adsorption of molecules of water [35]. At 232.6 eV, peak represented peroxo groups

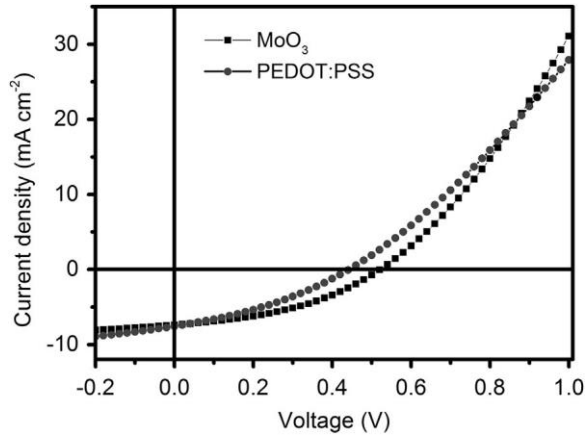

Fig. 6. Curve of the current density versus potential (J vs V) of the inverted organic solar cell of MoO_3_Cz and PEDOT:PSS deposited for spin coating at 1000 rpm.

(O_2^{2-}) connected to the Mo atom relating to surface defects [35]. The stoichiometry of the MoO_3_Cz oxide was calculated from the peak areas of Mo 3d and O 1s spectra and is given in Table 2. Thus, the molecular formula should be precisely expressed as MoO_{3-x}, where x represents the number of oxygen vacancies [38]. The non stoichiometric ratio can be related to the presence of Mo^{+5} ions. The supposed general values of atomic percentage of oxygen and molybdenum were 71.718% ± 0.202 e 28.281% ± 0.202, respectively. Thereby, the ratio between this atoms was 2,53, and the general molecular formula should be written as $MoO_{2,53}$.

UPS spectra, Tauc's method applied to UV−VIS−NIR spectrum and energy level diagram are shown in Fig. 5. Fig. 5a shows the UPS spectrum, the emission onset and secondary electron cutoff position were obtained with regard to the Fermi energy of gold film. The values provided by work function and ionized potential were 4.61 ± 0.01 eV and 7.75 ± 0.01 eV, respectively. It is known from the literature that the presence of Mo^{5+} species may result in the formation of isolated, occupied gap states close to the conduction band [39]. These states can cause the Fermi level to shift upwards and consequently reduce the work function [40].

Absorption spectrum (insert Fig. 5b) was studied to determine the optical band gap, by using the Tauc's method (Fig. 5b). We could observe in inset of Fig. 5b, the presence of optical absorptions in the visible and near-infrared wavelength region, which could be associated with oxygen vacancies and the presence of reduced Mo^{5+} species states in MoO_{3-x} [39], such as also observed by HRTEM and XPS. The main characteristic of an oxygen deficient material is the increase of the free electron concentration [38]. Usually, it can be evidenced by an increase in the conductivity and a strong optical absorption [40,41]. Furthermore, the oxygen ion vacancies of the MoO_{3-x} are occupied by two electrons and acted as donor centers and the charge transfer from oxygen vacancies to Mo ions creates reduced states of Mo^{+5} [40]. The low work function could be related with amount of Mo^{+5} species. It can be responsible to influence the built-in electric field of the devices and the photocurrent being extracted at short-circuits with low efficiency [40]. Note that the band gap from Tauc's method (Fig. 5b) for MoO_3_Cz was 3.33 ± 0.21 eV and corroborated with the values described in the literature for MoO_3 of 3.1 eV [42,43].

Combining the information above and the calculated conductive band, or electron affinities, by subtracting the band gap energy from ionized potential to be 4.42 eV [44], the energy levels diagram MoO3_Cz was constructed and it is presented in the Fig. 5c. The Fermi level is located near the conduction band, indicating that this material shows characteristic of an n-type semiconductor. This behavior can be explained by the presence of oxygen vacancies [42,44], as shown by the characterization techniques above discussed. Although UPS data indicate that the material was an n-type semiconductor, it still has hole transport properties in solar cells [42].

3.2. Inverted organic solar cell

The deposition speed of the MoO_3_Cz dispersion was optimized by testing in triplicate with 5 different speed and their standard deviation, the results are summarized in Table 3. The deposition speed has direct influence in the thickness of MoO_3 layer, and it plays a critical role for effective utilization of the HTL in an inverted OSC [45]. We can observe similar cell parameter for 500 and 2000, and the same effect can be observed for 1000 and 3000 rpm. It is known that the

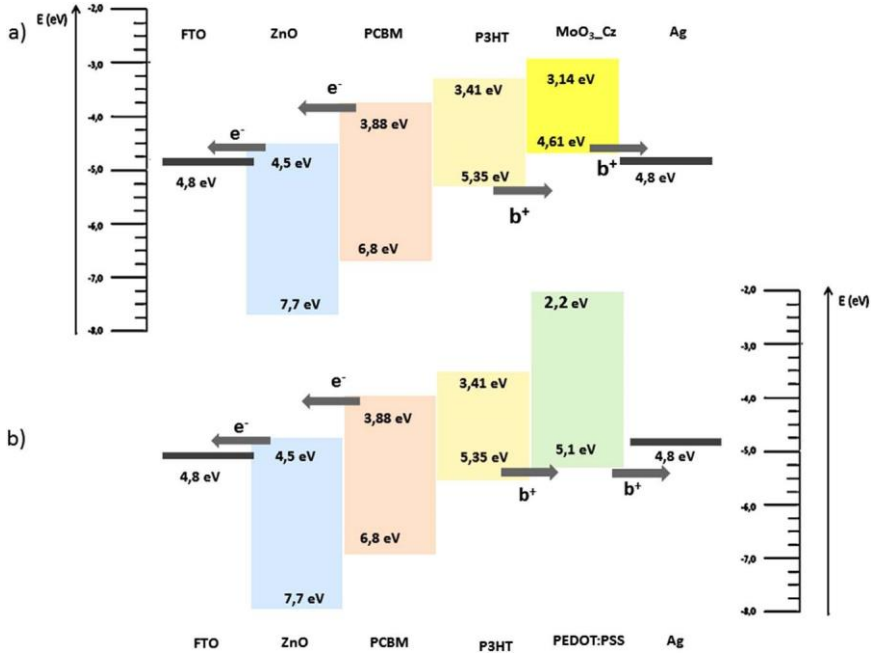

Fig. 7. Schematic representation of the band energy diagram alignment for the inverted organic solar cell a) FTO/ZnO/PCBM:P3HT/MoO_3_Cz/Ag and b) FTO/ZnO/PCBM:P3HT/ PEDOT:PSS/Ag.

HTL should be thick enough to act as a protection layer, preventing the Ag diffusion into the active layer [40]. Therefore, the spin coating speed of the 1000 rpm was chosen to allow the best parameters for solar cell and to show the lowest standard deviation with higher reproducibility. Table 4 gives the observed values obtained for devices: FTO/ZnO/PCBM:P3HT/MoO_3_Cz/Ag and FTO/ZnO/PCBM:P3HT/ PEDOT:PSS/Ag, which are also shown in graphical form in Fig. 6. Note that the device containing MoO_3_Cz presented higher efficiency (PCE), fill factor (FF) and current open circuit (V_{oc}), showing that the material has potential to be used as hole carrier in reverse and organic solar cells, replacing the PEDOT:PSS. The improved FF value in the MoO_3_Cz device could be associated in part with a low in series resistance (Rs), 24.05 and 28.65 Ω cm^2, respectively to MoO_3_Cz and PEDOT:PSS, indicating an improvement in charge transport [35,41]. In this case, the V_{oc} value of the MoO_3_Cz device is higher than PEDOT:PSS, it could be related the value of the parallel shunt resistance (Rsh) to be low to the MoO_3_Cz device. The ideal condition is that R_{sh} be as high as possible, so that the current can be transferred to the contacts of the device and not dissipated in internal losses. In these aspects, the V_{oc} values is its relation to the organization of the active layer, but as diffusion processes of MoO_3 or PEDOT:PSS and/or Ag in the active layer can also be involved in this step, this could involve recombination processes reducing the stability of these devices [46], these processes occur mainly due to the presence of Mo^{5+} species, as seen by XPS analysis.

However, the PEDOT:PSS presented higher short circuit current value density (J_{sc}) (7.541 mA cm^{-2}) than MoO_3_Cz (7.386 mA cm^{-2}). This value might be related to the conductive nature of the hole carrier layer, and it was one more indication of the non-stoichiometric nature of MoO_3_Cz [46], corroborating the previous data. Hammond and colleagues [41] observed that the reduction in Jsc, could be attributed in part to the decreased optical transmission of the MoO_3 layer as compared to the PEDOT:PSS layer, and also to the charge recombination at Mo^{5+} gap states.

The values obtained for this solar cells were lower when compared to the same configuration previously reported in the literature [39], especially the FF value. However, it is important to emphasize that there could be variations in some fabrication conditions of this device in this study and there is a need optimization of devices fabrication or more experimental data. In this case we want to show that is possible replace the PEDOT:PSS by MoO_3_Cz.

Fig. 7 shows the schematic bands diagram for inverted organic solar cell. The hole blocker, ZnO, collects electrons from the acceptor PCBM and send it to the anode, FTO. The hole is generated and transported through the P3HT layer, toward the PEDOT:PSS/MoO_3_Cz. The work function of the ZnO and PEDOT:PSS/MoO_3_Cz are near to HOMO of PCBM and LUMO of P3HT, respectively. This allows for efficient injection of electrons into the layer of ZnO, as well as the collection of holes by PEDOT:PSS/MoO_3_Cz [47]. Note that the conduction band of PEDOT:PSS (Fig. 7a) is higher than MoO_3_Cz (Fig. 7b) it makes more difficult for hole collection by the Ag layer, which may explain the higher efficiency in solar cell using the MoO_3_Cz compared to PEDOT:PSS.

4. Conclusions

α-MoO_3 was successfully synthesized by refluxing MoS_2 in oxidant media (HNO_3/H_2SO_4 aqueous solutions). The structural and morphological characterizations indicated that it was obtained with reduced size, belt-type morphology, high phase purity and strongly-preferred orientation in the [001] direction. Furthermore, structural defects, observed by HRTEM and XPS, could be related to oxygen deficiency, allowing a wide variety of potential application, ensuring its multifunctionality. Inverted organic solar cells employing α-MoO_3 as hole transport layer (HTL) showed enhanced values of PCE, FF and V_{oc} in comparison with PEDOT:PSS reference device, showing that α-MoO_3 obtained in this study has potential to be used as hole transporter in this kind of devices and replacing PEDOT:PSS. Furthermore, the α-MoO_3 has the advantage of improve the device-stability under atmospheric conditions.

Acknowledgements

The authors acknowledge the financial support from CAPES, CNPq, FINEP and the Science Without Borders program from CNPq (Brazil) for the grants awarded to A.A.B (249144/2013-1). We also acknowledge to Dr. Monica Lira-Cantu and ICN2. A.A.B. acknowledge CAPES for fellowship.

References

[1] K.D. Parghi, R.V. Jayaram, Sequential oxidation and condensation of alcohols to benzimidazoles/benzodiazepines by MoO3–SiO2 as a heterogeneous bifunctional catalyst, Catal. Commun. 11 (2010) 1205–1210. http://dx.doi.org/10.1016/j.catcom.2010.07.008.

[2] G.P. Nagabhushana, D. Samrat, G.T. Chandrappa, α-MoO3 nanoparticles: solution combustion synthesis, photocatalytic and electrochemical properties, RSC Adv. 4 (2014) 56784–56790. http://dx.doi.org/10.1039/C4RA05135A.

[3] Y. Song, H. Wang, Z. Li, N. Ye, L. Wang, Y. Liu, HxMoO3@C nanobelts: green synthesis and superior lithium storage properties, Int. J. Hydrog. Energy 40 (2015) 3613–3623. http://dx.doi.org/10.1016/j.ijhydene.2015.01.027.

[4] Y.H. Cho, Y.N. Ko, Y.C. Kang, I.D. Kim, J.H. Lee, Ultraselective and ultrasensitive detection of trimethylamine using MoO3 nanoplates prepared by ultrasonic spray pyrolysis, Sens. Actuators B Chem. 195 (2014) 189–196. http://dx.doi.org/10.1016/j.snb.2014.01.021.

[5] T. Yunusi, C. Yang, W. Cai, F. Xiao, J. Wang, X. Su, Synthesis of MoO3 submicron belts and MoO2 submicron spheres via polyethylene glycol-assisted hydrothermal method and their gas sensing properties, Ceram. Int. 39 (2013) 3435–3439. http://dx.doi.org/10.1016/j.ceramint.2012.09.096.

[6] Y. Wang, Q. Luo, N. Wu, Q. Wang, H. Zhu, L. Chen, et al., Solution-processed MoO3:PEDOT:PSS hybrid hole transporting layer for inverted polymer solar cells, ACS Appl. Mater. Interfaces (2015). http://dx.doi.org/10.1021/am509049t.

[7] J. Chen, M. Wang, X. Liao, Z. Liu, J. Zhang, L. Ding, et al., Large-scale synthesis of single-crystal molybdenum trioxide nanobelts by hot-wire chemical vapour deposition, J. Alloy. Compd. 619 (2015) 406–410. http://dx.doi.org/10.1016/j.jallcom.2014.09.069.

[8] S. Bai, C. Chen, Y. Tian, S. Chen, R. Luo, D. Li, et al., Facile synthesis of a-MoO3 nanorods with high sensitivity to CO and intrinsic sensing performance, Mater. Res. Bull. 64 (2015) 252–256. http://dx.doi.org/10.1016/j.materresbull.2014.12.049.

[9] S. Murase, Y. Yang, Solution processed MoO 3 interfacial layer for organic photovoltaics prepared by a facile synthesis method, Adv. Mater. 24 (2012) 2459–2462. http://dx.doi.org/10.1002/adma.201104771.

[10] J. Dagar, P. Tyagi, R. Ahmad, R. Singh, O.P. Sinha, C.K. Suman, et al., Application of 2D-MoO3 nano-flakes in organic light emitting diodes: effect of semiconductor to metal transition with irradiation, RSC Adv. 5 (2014) 8397–8403. http://dx.doi.org/10.1039/C4RA12430H.

[11] A. Iwan, M. Palewicz, I. Tazbir, B. Boharewicz, R. Pietruszka, M. Filapek, et al., Influence of ZnO:Al, MoO3 and PEDOT:PSS on efficiency in standard and inverted polymer solar cells based on polyazomethine and poly(3-hexylthiophene), Electrochim. Acta 191 (2016) 784–794. http://dx.doi.org/10.1016/j.electacta.2016.01.107.

[12] P.-Y. Ho, J.-Y. Sun, S.-H. Kao, C.-Y. Kao, S.-H. Lin, S. Lan, et al., The effects of MoO3 treatment on inverted PBDTTT-C:PC71BM solar cells, Sol. Energy Mater. Sol. Cells 119 (2013) 235–240. http://dx.doi.org/10.1016/j.solmat.2013.07.048.

[13] G. Terán-Escobar, J. Pampel, J.M. Caicedo, M. Lira-Cantú, Low-temperature, solution-processed, layered V2O5 hydrate as the hole-transport layer for stable organic solar cells, Energy Environ. Sci. 6 (2013) 3088. http://dx.doi.org/10.1039/ c3ee42204f.

[14] X. Zeng, X. Zhang, M. Yang, Y. Qi, A facile hydrothermal method for the fabrication of one-dimensional MoO3 nanobelts, Mater. Lett. 112 (2013) 87–89. http://dx.doi.org/10.1016/j.matlet.2013.08.130.

[15] G. Li, C. Li, H. Tang, K. Cao, J. Chen, F. Wang, et al., Synthesis and characterization of hollow MoS2 microspheres grown from MoO3 precursors, J. Alloy. Compd. 501 (2010) 275–281. http://dx.doi.org/10.1016/j.jallcom.2010.04.088.

[16] G. Wei, W. Qin, D. Zhang, G. Wang, R. Kim, K. Zheng, et al., Synthesis and field emission of MoO3 nanoflowers by a microwave hydrothermal route, J. Alloy. Compd. 481 (2009) 417–421. http://dx.doi.org/10.1016/j.jallcom.2009.03.007.

[17] D. Hanlon, C. Backes, T.M. Higgins, M. Hughes, A. O'Neill, P. King, et al., Production of molybdenum trioxide nanosheets by liquid exfoliation and their application in high-performance supercapacitors, Chem. Mater. 26 (2014) 1751–1763. http://dx.doi.org/10.1021/cm500271u.

[18] J. Gong, W. Zeng, H. Zhang, Hydrothermal synthesis of controlled morphologies of MoO3 nanobelts and hierarchical structures, Mater. Lett. 154 (2015) 170–172. http://dx.doi.org/10.1016/j.matlet.2015.04.092.

[19] P. Afanasiev, Synthetic approaches to the molybdenum sulfide materials, C. R. Chim. 11 (2008) 159–182. http://dx.doi.org/10.1016/j.crci.2007.04.009.

[20] T.R. Andersen, H.F. Dam, B. Andreasen, M. Hösel, M.V. Madsen, S.A. Gevorgyan, et al., A rational method for developing and testing stable flexible indium- and vacuum-free multilayer tandem polymer solar cells comprising up to twelve roll processed layers, Sol. Energy Mater. Sol. Cells 120 (2014) 735–743. http://dx.doi.org/10.1016/j.solmat.2013.07.006.

[21] F. Wypych, Dissulfeto de molibdênio, um material multifuncional e surpreendente, Quim. Nova 25 (2002) 83–88 ⟨http://www.scielo.br/scielo.php?script=sci_arttext & pid=S0100-40422002000100015 & nrm=iso⟩.

[22] L. Sui, Y.-M. Xu, X.-F. Zhang, X.-L. Cheng, S. Gao, H. Zhao, et al., Construction of three-dimensional flower-like α-MoO3 with hierarchical structure for highly selective triethylamine sensor, Sens. Actuators B Chem. 208 (2015) 406–414. http://dx.doi.org/10.1016/j.snb.2014.10.138.
[23] H. Sinaim, D.J. Ham, J.S. Lee, A. Phuruangrat, S. Thongtem, T. Thongtem, Freepolymer controlling morphology of a-MoO3 nanobelts by a facile hydrothermal synthesis, their electrochemistry for hydrogen evolution reactions and optical properties, J. Alloy. Compd. 516 (2012) 172–178. http://dx.doi.org/10.1016/ j.jallcom.2011.12.024.
[24] U.K. Sen, S. Mitra, Electrochemical activity of α-MoO3 nano-belts as lithium-ion battery cathode, RSC Adv. 2 (2012) 11123. http://dx.doi.org/10.1039/c2ra21373g.
[25] Z. Wang, S. Madhavi, X.W. Lou, Ultralong a-MoO3 nanobelts: synthesis and effect of binder choice on their lithium storage properties, J. Phys. Chem. C 116 (2012) 12508–12513. http://dx.doi.org/10.1021/jp304216z.
[26] Y. Li, T. Liu, T. Li, X. Peng, Hydrothermal fabrication of controlled morphologies of MoO3 with CTAB: structure and growth, Mater. Lett. 140 (2015) 48–50. http://dx.doi.org/10.1016/j.matlet.2014.10.153.
[27] S. Vidya, S. Solomon, J.K. Thomas, Synthesis and characterisation of MoO3 and WO3 nanorods for low temperature co-fired ceramic and optical applications, J. Mater. Sci. Mater. Electron. 26 (2015) 3243–3255. http://dx.doi.org/10.1007/ s10854-015-2823-8.
[28] Y. Ma, X. Zhang, M. Yang, Y. Qi, Controlled growth of MoO3 nanorods on transparent conducting substrates, Mater. Lett. 136 (2014) 146–149. http://dx.doi.org/10.1016/j.matlet.2014.07.143.
[29] B. Windom, W. Sawyer, D. Hahn, A raman spectroscopic study of MoS2 and MoO3: applications to tribological systems, Tribol. Lett. 42 (2011) 301–310. http://dx.doi.org/10.1007/s11249-011-9774-x.
[30] H. Li, Q. Zhang, C.C.R. Yap, B.K. Tay, T.H.T. Edwin, A. Olivier, et al., From bulk to monolayer MoS2: evolution of Raman scattering, Adv. Funct. Mater. 22 (2012) 1385–1390. http://dx.doi.org/10.1002/adfm.201102111.
[31] N. Illyaskutty, S. Sreedhar, G. Sanal Kumar, H. Kohler, M. Schwotzer, C. Natzeck, et al., Alteration of architecture of MoO_3 nanostructures on arbitrary substrates: growth kinetics, spectroscopic and gas sensing properties, Nanoscale 6 (2014) 13882–13894. http://dx.doi.org/10.1039/C4NR04529G.
[32] S. Bai, S. Chen, L. Chen, K. Zhang, R. Luo, D. Li, et al., Ultrasonic synthesis of MoO 3 nanorods and their gas sensing properties, Sens. Actuators B Chem. 174 (2012) 51–58. http://dx.doi.org/10.1016/j.snb.2012.08.015.
[33] K. Ajito, L.A. Nagahara, D.A. Tryk, K. Hashimoto, A. Fujishima, Study of the photochromic properties of amorphous MoO3 films using Raman microscopy, J. Phys. Chem. 99 (1995) 16383–16388. http://dx.doi.org/10.1021/j100044a028.
[34] O. Lupan, V. Cretu, M. Deng, D. Gedamu, I. Paulowicz, S. Kaps, et al., Versatile growth of freestanding orthorhombic α-molybdenum trioxide nano- and microstructures by rapid thermal processing for gas nanosensors, J. Phys. Chem. C 118 (2014) 15068–15078. http://dx.doi.org/10.1021/jp5038415.
[35] A.M. Douvas, M. Vasilopoulou, D.G. Georgiadou, A. Soultati, D. Davazoglou, N. Vourdas, et al., Sol-gel synthesized, low-temperature processed, reduced molybdenum peroxides for organic optoelectronics applications, J. Mater. Chem. C 2 (2014) 6290–6300. http://dx.doi.org/10.1039/C4TC00301B.
[36] P. Jittiarporn, L. Sikong, K. Kooptarnond, W. Taweepreda, Effects of precipitation temperature on the photochromic properties of h-MoO3, Ceram. Int. 40 (2014) 13487–13495. http://dx.doi.org/10.1016/j.ceramint.2014.05.076.
[37] J. Zhou, N. Lin, L. Wang, K. Zhang, Y. Zhu, Y. Qian, Synthesis of hexagonal MoO3 nanorods and a study of their electrochemical performance as anode materials for lithium-ion batteries, J. Mater. Chem. A 3 (2015) 7463–7468. http://dx.doi.org/10.1039/C5TA00516G.
[38] M.M.Y.A. Alsaif, M.R. Field, T. Daeneke, A.F. Chrimes, W. Zhang, B.J. Carey, et al., Exfoliation solvent dependent plasmon resonances in two-dimensional sub-stoichiometric molybdenum oxide nanoflakes, ACS Appl. Mater. Interfaces 8 (2016) 3482–3493. http://dx.doi.org/10.1021/acsami.5b12076.
[39] H. Zhang, A. Borgschulte, F.A. Castro, R. Crockett, A.C. Gerecke, O. Deniz, et al., Photochemical transformations in fullerene and molybdenum oxide affect the stability of bilayer organic solar cells, Adv. Energy Mater. 5 (2015). http://dx.doi.org/10.1002/aenm.201400734.
[40] Y. Li, H. Yu, X. Huang, Z. Wu, M. Chen, A simple synthesis method to prepare a molybdenum oxide hole-transporting layer for efficient polymer solar cells, RSC Adv. 7 (2017) 7890–7900. http://dx.doi.org/10.1039/C7RA00303J.
[41] S.R. Hammond, J. Meyer, N.E. Widjonarko, P.F. Ndione, A.K. Sigdel, A. Garcia, et al., Low-temperature, solution-processed molybdenum oxide hole-collection layer for organic photovoltaics, J. Mater. Chem. 22 (2012) 3249–3254. http://dx.doi.org/10.1039/C2JM14911G.
[42] G. Wang, T. Jiu, P. Li, J. Li, C. Sun, F. Lu, et al., Preparation and characterization of MoO3 hole-injection layer for organic solar cell fabrication and optimization, Sol. Energy Mater. Sol. Cells 120 (2014) 603–609. http://dx.doi.org/10.1016/j.solmat.2013.10.002.
[43] a.H. Reshak, Specific features of electronic structures and optical susceptibilities of molybdenum oxide, RSC Adv. 5 (2015) 22044–22052. http://dx.doi.org/10.1039/C5RA00081E.
[44] K.H. Wong, K. Ananthanarayanan, J. Luther, P. Balaya, Origin of hole selectivity and the role of defects in low-temperature solution-processed molybdenum oxide interfacial layer for organic solar cells, J. Phys. Chem. C 116 (2012) 16346–16351. http://dx.doi.org/10.1021/jp303679y.
[45] S.O. Oseni, G.T. Mola, Properties of functional layers in inverted thin film organic solar cells, Sol. Energy Mater. Sol. Cells 160 (2017) 241–256. http://dx.doi.org/10.1016/j.solmat.2016.10.036.
[46] S. Chambon, L. Derue, M. Lahaye, B. Pavageau, L. Hirsch, G. Wantz, MoO3 thickness, thermal annealing and solvent annealing effects on inverted and direct polymer photovoltaic solar cells, Materials (Basel) 5 (2012) 2521–2536. http:// dx.doi.org/10.3390/ma5122521.
[47] J. Weickert, H. Sun, C. Palumbiny, H.C. Hesse, L. Schmidt-Mende, Spray-deposited PEDOT:PSS for inverted organic solar cells, Sol. Energy Mater. Sol. Cells 94 (2010) 2371–2374. http://dx.doi.org/10.1016/j.solmat.2010.08.018.